Postprint of: Skarżyński Ł., Tejchman J., Experimental investigations of damage evolution in concrete during bending by continuous micro-CT scanning, Materials Characterization, Vol. 154 (2019), pp. 40-52, DOI: 10.1016/j.matchar.2019.05.034

Experimental investigations of damage evolution in concrete during bending by continuous micro-CT scanning

Ł. Skarżyński and J. Tejchman

Faculty of Civil and Environmental Engineering, Gdańsk University of Technology, Poland

lskarzyn@pg.edu.pl, tejchmk@pg.gda.pl

Abstract

The paper describes experimental investigation results of fracture in notched concrete beams under quasi-static three-point bending. To visualize 3D fracture in concrete under bending, an extended X-ray micro-computed tomography system was used, i.e. the tomography system SkyScan 1173 was connected to the loading machine ISTRON 5569. This combined system enabled to shot images of deforming concrete beams during a continuous deformation process, i.e. without beams' unloading for scanning. The shape, volume, size of cracks and pores were non-destructively measured during deformation. The maximum crack width during continuous micro-CT scanning was higher by about 30% than in the beam that was subjected to unloading for scanning.

Keywords: bending; concrete; pores; fracture; continuous scanning; X-ray micro-CT

1. Introduction

Concrete is the most widely used construction material in the world in terms of volume since it has the lowest ratio between cost and strength as compared to other available engineering materials. It is a complex material with a random heterogeneous multi-phase structure. Its main constituents at the meso-scale are cement matrix, aggregate, voids and interfacial transitional zones (ITZs) between the aggregate and cement matrix. Fracture is a phenomenon of the major importance in concrete ([1]-[4]). During fracture, micro-cracks first arise in a hardening region on the stress-strain curve and then evolve during material softening into dominant distinct macro-cracks. The fracture process in concrete is strictly connected with its heterogeneous structure that varies from the few nanometres (hydrated cement) to the millimetres (aggregate particles). Thus, to optimize the concrete behaviour

and to make sure the safety of concrete and reinforced concrete structures, the understanding of a fracture process at the aggregate level is of major importance. Different experimental techniques were used in the past to investigate a fracture process in concrete (scanning electron microscopy, high-speed photography, laser speckle, interferometry, acoustic emission, X-ray technique and digital image correlation (DIC) technique) by considering a spatial distribution of constituents to investigate more accurately the material properties of concrete. At present, the most effective technique is the three-dimensional (3D) X-ray micro-computed tomography (in short 'micro-CT') technology which now is being used widely in experimental mechanics research to non-destructively study the 3D material micro-structure and its evolution during deformation with high-resolution ([5-7]). It is a powerful non-destructive tool that is able to define the density of each specimen voxel by assigning a shade of grey according to the voxel density (light shades of grey correspond to high densities and dark shades of grey correspond to low densities). Thus the various constitutive phases can be segmented based on their relative X-ray attenuation rates and three-dimensional (3D) damage maps may be generated which helps to better understand the internal mechanics of various materials. There is now no other alternative that can reach such a high level of accuracy as micro-CT.

The presented research work is experimentally oriented. The main aim of this experimental study is to offer the detailed information on a 3D geometric characterization of aggregate particles, pores and cracks in concrete and their evolution during 3-point bending using a very advanced extended X-ray micro-computed tomography system. The 3-point bending test is the conventional method of measuring the mechanical behaviour of concrete under tension [8]. In contrast to existing X-ray micro-CT measurements wherein unloading breaks are needed for scanning, the concrete specimens were now loaded and continuously scanned without any crack recovery effects (which represents the most relevant novelty in our paper). The very advanced micro-CT system SkyScan 1173 was employed [5] that was connected to the loading machine INSTRON 5569. The 3-point bending experiments consisted of two basic steps. In the first step, the effect of the beam unloading on the crack width was investigated. In the second step, some 3D damage maps were reconstructed during continuous bending. The micro-CT scans were made for 3 loading points. They gave information about a real volumetric distribution, shape and size of voids and cracks in concrete. Our experimental results may be very helpful for the calibration of different models within continuum and discrete mechanics dealing with fracture [1-4]. Similar micro-CT scans of the internal microstructure, crack mechanisms and structural behaviour after bending tests on fiber-reinforced concrete were shot by Vicente et. al [7]. However, the scans were shot on unloaded specimens after the test. Our micro-CT scans were made during a continuous deformation process without

unloading breaks. The micro-CT scanning during continuous deformation has not been performed for concrete yet to our knowledge.

This paper is arranged as follows: The experimental procedure is presented in Section 2, the results of the tests are described and discussed in Section 3, and finally, the conclusions are offered in Section 4.

2. X-ray micro-CT system

Micro-computed tomography is a 3D imaging non-destructive technique using X-rays to see the inside of objects [5-6]. It was introduced in the 1980s. The micro-CT scanner makes a series of 2D planar X-ray images and reconstructs the data into 2D cross-sectional slices that are further processed into 3D models. Thus the quantitative volumetric information about changes in the internal micro/meso-structure may be obtained. This knowledge is important to better understand a fracture process. There are many examples of the use of micro-CT systems for concrete members (e.g. [9-19]). Our tomography system SkyScan 1173 was already successfully used for measuring the evolution of a fracture process in concrete during different quasi-static monotonic tests like bending [20], uniaxial compression [21], splitting [22-23] and in fibrous concrete during wedge splitting [24]. It was also used for concrete in compressive fatigue tests [25]. In the bending test [20], the damaged concrete specimen was cut out from the beam after the test for micro-CT scanning. In our experiments, the high energy table scanner SkyScan 1173 with the 130 keV microfocus X-ray source and flat panel sensor of the large format (5 Mpx) was used (Fig.1). It possessed special protection by a lead-glass fibre-optic window for achieving a long lifetime under the high X-ray energy. The scanner was additionally equipped with a precision object manipulator with the integrated micro-positioning stage. The pixel size can vary from 3 μm up to 90 μm. Several scanner filters were available in the front of the X-ray detector: 0.25 mm brass filter, 1.0 aluminium filter, 2.0 mm lead filter and 0.25 copper filter. Its main advantage was the possibility to scan large and dense objects with a diameter up to 200 mm. This micro-CT system was described in detail in [5]. However, all scanning processes were solely done after the specimens' unloading. The micro-CT images of the concrete structure allowed next to develop a very effective 3D 4-phase concrete model (composed of aggregate, cement matrix, macro-voids and ITZs) within discrete and continuum mechanics to faithfully reproduce the experimental cracks (place, shape, width) and mobilized strength in plain concrete. The 4-phase concrete model was used in DEM [20-23], [26], FEM with cohesive elements [27-28] and FEM within enhanced damage mechanics [20].

In the current paper, the scanning process was continuously performed during deformation without any unloading phases for concrete. The same tomography system SkyScan 1173 was used. However, it was directly connected now to the loading machine Instron 5569 (with the maximum loading capacity of 50 kN). The micro-CT scanner was mounted on the loading machine (Fig.2a). To rotate the specimen for scanning, a rotating frame was built and a stepper motor was used (Figs.2b and 2c) that were both fully controlled by the micro-CT software. Thus, the micro-CT scans might be shot during a very slow quasi-static deformation process without any breaks. The disadvantages of our extended prototype micro-CT system were two: 1) reduced scanning resolution (the pixel size was now between 39 μm and 46 μm) and 2) reduced maximum size of the scanned concrete specimen (now down to 80 mm).

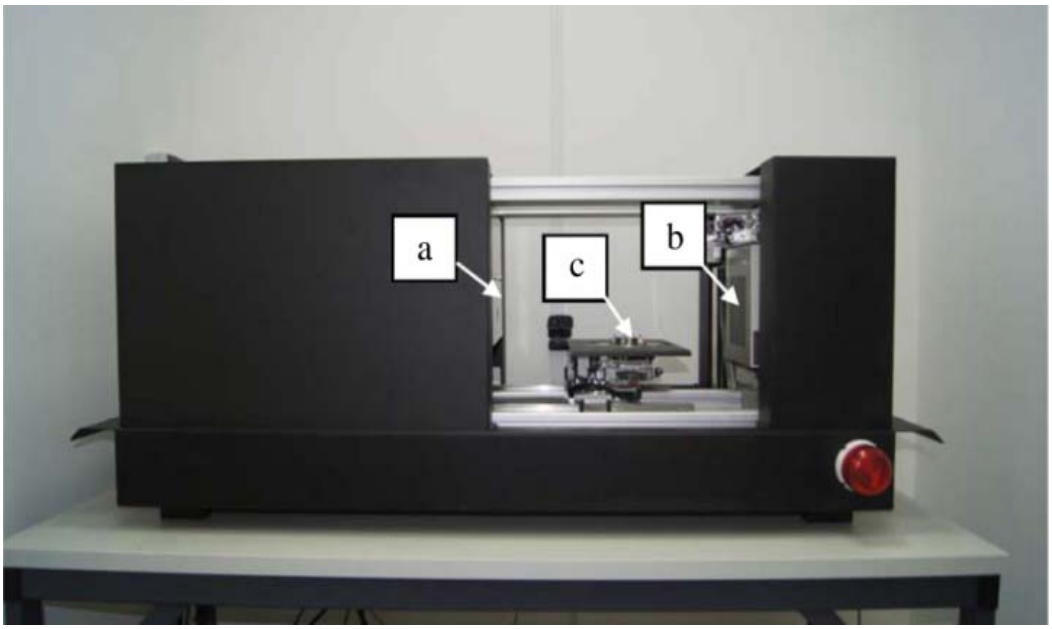

Fig.1: X-ray micro-computed tomography system SkyScan 1173: a) X-ray source, b) flat panel and c) precision object manipulator [4]

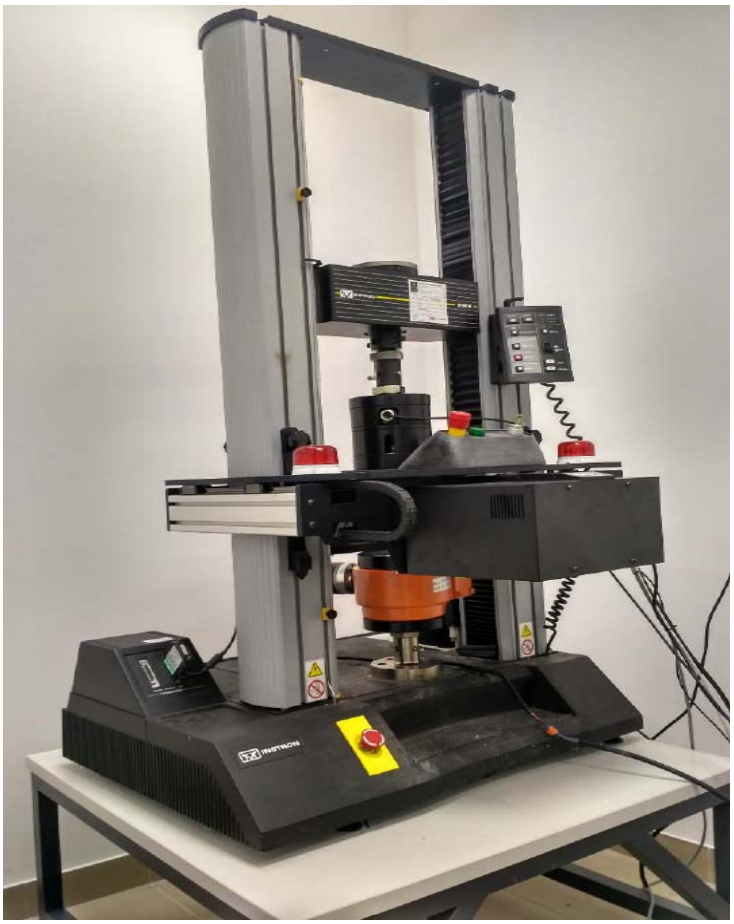

a)

b)

c)

Fig.2: Views on micro-CT tomography system Skyscan 1173 mounted to loading machine Instron 5569: a) general view, b) rotating frame (marked with arrows) with concrete specimen prepared for bending and c) stepper motor

2. Beam preparation and experiments

Beam preparation

The experimental program was carried out at the laboratory of the Gdańsk University of Technology. The beams were made from a single self-compacting concrete, including the river sand and gravel (round-shaped) aggregate particles of the maximum diameter of d_{max}=16 mm and cement CEM I 32.5R. The water/cement ratio was equal to w/c=0.42, particle volume was β=75% and aggregate volume ($d_a \geq$ 2 mm) was 50% (Fig.3). The amount of mixing components is presented in Tab.1. To improve the workability of the fresh concrete, a small amount of superplasticizer was added. The rectangular concrete beams (length L=80 mm, height D=40 mm and width b=40 mm), with a notch of the height $D/10$=4 mm and width of 3 mm situated at the beam mid-span (Fig.4), were cut out on the 28th day after concreting from the prism of 1000×1000 mm^2 in cross-section and 300 mm in total length (with the tolerance of ±0.2 mm). A relatively small concrete specimen was used to be entirely visible in the field of scanning of the micro-CT system. The ratio between the beam span and height was 60/40=1.5 (Fig.4) and twice smaller than for conventional specimens in 3-point bending testing in the standard EN 12390-5 [8]. For the ratio of 3, the beam height would be too small. For the first 7 days, the prism was properly cured to avoid the surface evaporation and autogeneous shrinkage. Based on some preliminary tests, the average uniaxial compressive strength was f_c=51.81 MPa with the standard deviation of 3.36 MPa (tested on 3 cubic concrete specimens 10×10×10 cm^3), the Young's modulus E=36.1 GPa with the standard deviation of 2.29 GPa and the Poisson's ratio υ=0.22 with the standard deviation of 0.03 (tested on 3 cylinder concrete specimens 15×30 cm^2). The mean tensile strength during bending was f_t=4.04 MPa with the standard deviation of 0.24 MPa (tested on 3 concrete beams 160×40×40 mm^2).

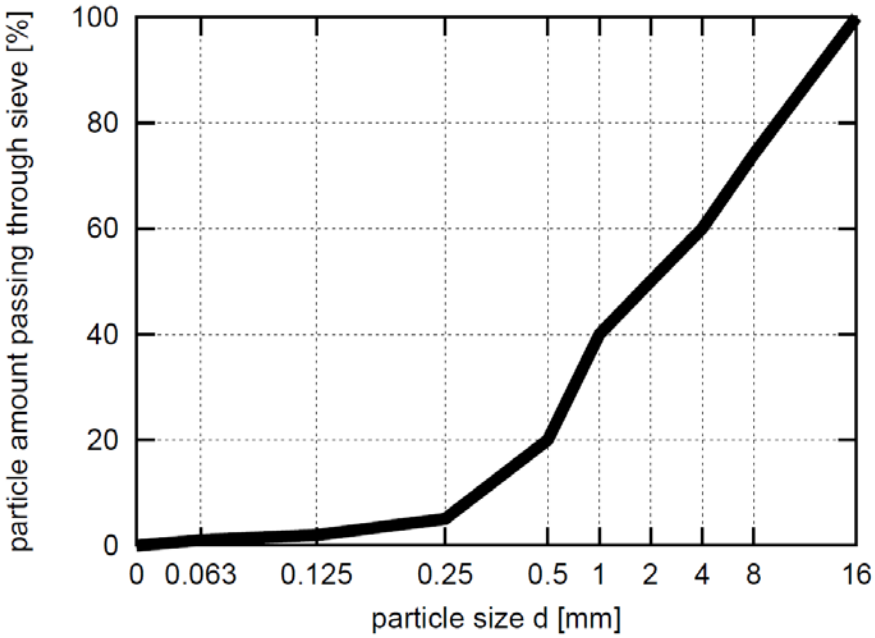

Fig.3: Particle size distribution curve of concrete (mean particle diameter d_{50}=2 mm and maximum particle diameter d_{max}=16 mm)

Tab.1: Concrete mix components in experiments (d_{50} – mean particle diameter, d_{max} – maximum particle diameter, β – particle volume)

Concrete components	**Amount** (d_{50}=2 mm, d_{max}=16 mm, β=75%)
cement (Portland 32.5R)	810 kg/m^3
sand (0 - 2 mm)	650 kg/m^3
gravel aggregate (2 - 8 mm)	580 kg/m^3
gravel aggregate (8 - 16 mm)	580 kg/m^3
Water	340 l/m^3

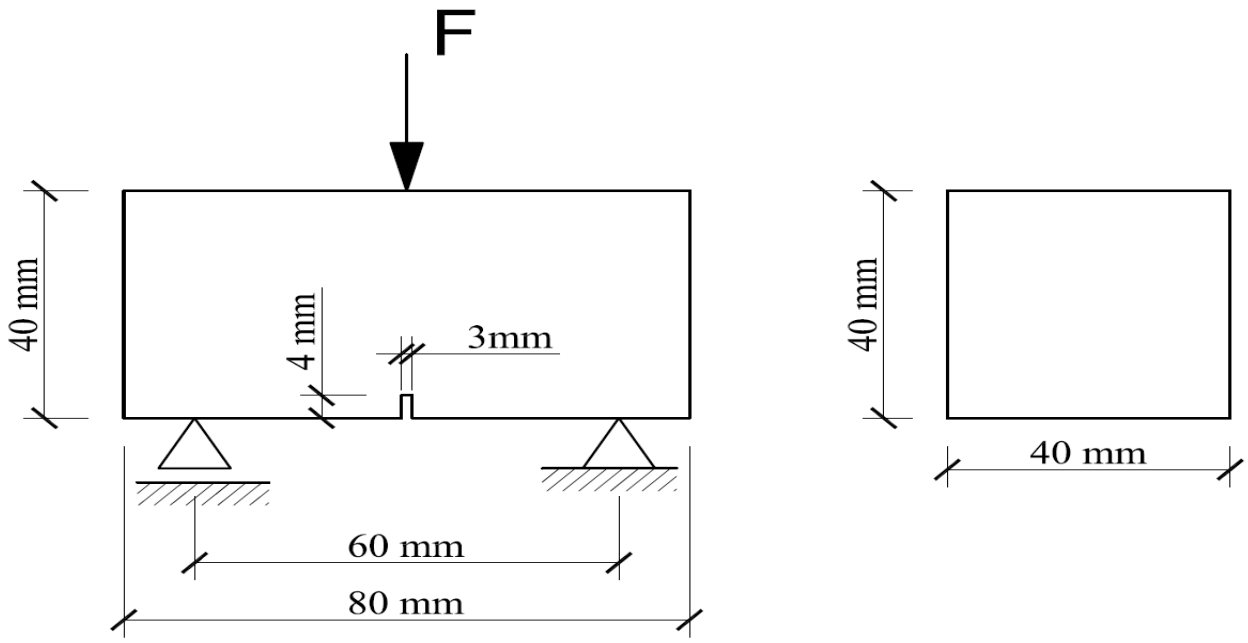

Fig.4: Geometry of experimental concrete beams 80×40×40 m^3 subjected to three-point bending (*F* - vertical force)

Experiments

The quasi-static test with concrete beam under 3-point bending was performed with a controlled notch opening displacement rate CMOD (crack mouth opening displacement) of 0.001 mm/min. A CMOD gauge with the length of 5 mm at the notch at the beam bottom. The gauge precision was 0.0025 mm at the maximum permissible axial displacement of 2 mm. The test ended for the CMOD≈0.25 mm. Before each experiment, the initial 3D micro-CT scans of concrete beams were made. The experiments consisted of 2 main steps. In the first step, to investigate the effect of unloading on the crack behaviour, the 3D scans of two concrete beams (called '1' and '2') were made at the end of three-point bending tests. One beam (called '3') was scanned under the existing residual force and the second one was scanned after beam unloading. In the second step, the fracture evolution was investigated during a continuous bending process. The concrete beam '3' was scanned 3 times: a) in the pre-peak regime, b) in the post-peak softening region and c) close to the failure. The deformation process was continuous and not stopped during each scanning phase (that lasted about 1 hour). The deformation continuously increased but extremely slowly. Note that the micro-CT images for the beams '1' and '2' should be taken on the same beam to precisely determine the effect of unloading. However, due to the similar concrete of the beams '1' and '2' with a similar initial porosity (Tab.2), the effect of unloading was found, based on two separate tests with the beams '1' and '2'. Since the deformation process was continuous, it was crucial to reduce

the scanning time but to simultaneously keep the high image quality. In order to fulfil these two requirements, many preliminary scanning tests were carried out. Finally, the X-ray source voltage of the micro-CT scanner was assumed to be 130 keV, the current was 61 μA and exposure time was equal to 400 ms. The pixel size of the micro-CT was 39.68 μm. The X-ray projections were recorded with the rotation increment of 0.2°. To diminish the noise in X-ray projections, the frame averaging option was set to be 2 and random movement option was 4. In order to distinguish pores and cracks from concrete, a threshold procedure was performed based on density differences of each concrete phase. In our experiments, the threshold in the range 0-70 was used. The single scanning time was one hour. All beams were scanned using the same set of parameters. The experiments lasted about five hours with one micro-CT image and seven hours with three micro-CT images. It is not possible to resolve the crack nucleation and initial growth with the scanning resolution of about 40 μm. To do it, the scanning resolution has to be about 2-3 μm that is related to the use of an extremely small concrete specimen (few millimetres large).

3. Experimental results

3.1 Effect of continuous and discontinuous micro-CT scanning on fracture

Table 2 includes the volumes of pores of the beams '1'-'3' which were also divided into open and closed pores. The open pores were defined as the pores which spread beyond the borders of the investigated beam and the closed pores were located in the beam interior. The cracks were always treated as the open pores. Figure 5a presents a general view on the initial 3D micro-CT scan of the entire non-cracked concrete beam '3' before the test. The 3D distribution of pores in the entire non-cracked concrete beam '3' is demonstrated in Fig.5b.

Tab.2: Volume of pores and distribution of pore diameters in non-cracked concrete beams at beginning of tests

Beam number	**Diameter range of all pores [%]**				**Volume of all pores [mm^3]**	**%- volume of all pores [%]**	**%-volume of closed pore [%]**	**%-volume of open pore [%]**
	≤ 0.50 mm	0.51-1.00 mm	1.01-2.00 mm	≥ 2.01 mm				
1	12.3	17.4	34.5	35.8	3762.4	3.42	2.26	1.16
2	14.5	12.0	36.5	37.0	3575.5	3.25	2.40	0.85
3	10.2	11.1	32.5	46.2	4213.1	3.83	2.43	1.40

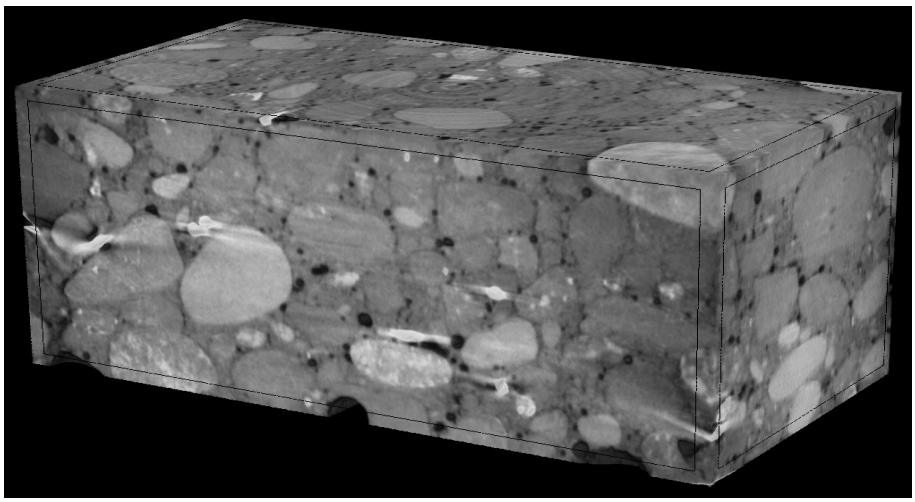

a)

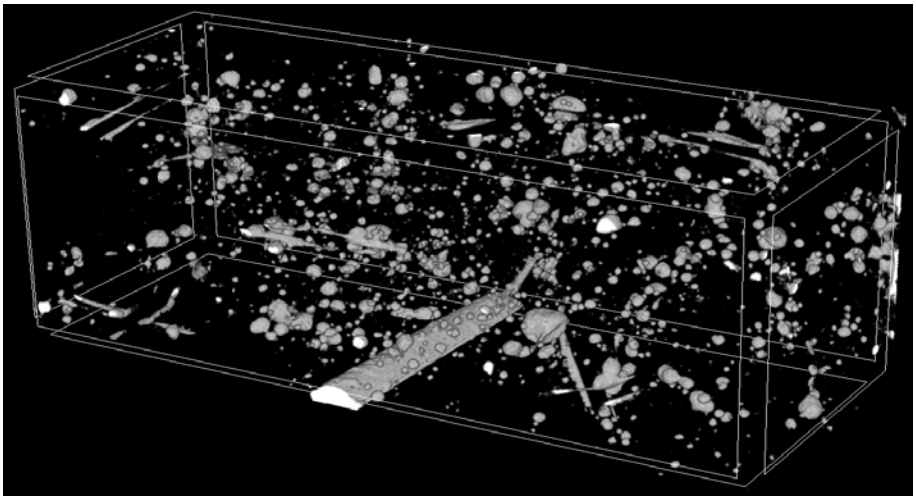

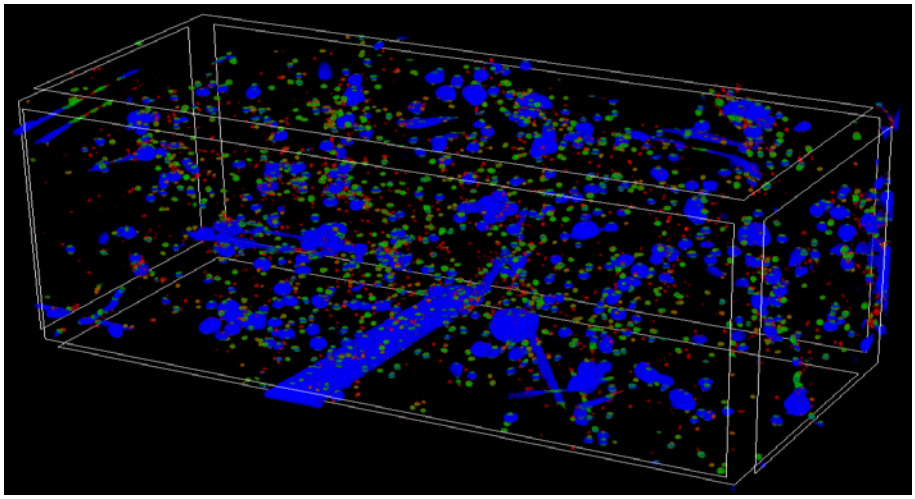

b)

Fig.5: 3D micro-CT images of non-cracked concrete notched beam '3' at beginning of test: a) external view on beam and b) internal distribution of pores without and with specified diameter (colours denote pore diameters in range of ≤1.0 mm (in red), 1.0-2.0 mm (in green) and ≥2.0 mm (in blue))

The heterogeneous 3D material meso-structure is well visible and 3 phases (aggregate particles, cement matrix and pores) are clearly visible in Fig.5a. The total volume of pores in the beam '3' was: 4213.1 mm^3, i.e. 3.83% of the total beam volume (2.43% - the closed pores and 1.40% - the open pores) (Tab.2). The total volume of pores in the remaining two beams was the following: 3762.4 mm^3, i.e. 3.42% of the total beam volume (2.26% - the closed pores and 1.16% were the open pores) in the beam '1' and 3575.5 mm^3, i.e. 3.25% of the total beam volume (2.40% - the closed pores and 0.85% were the open pores) in the beam '2' (Tab.2). Slightly various porosities of concrete in Tab.2 were due to non-uniform vibration of the fresh concrete mixture (the beams were cut out from different parts of the concrete prism). The pores with the diameter smaller than 1.0 mm constituted 20-35% of total pores (so-called 'micro-pores'), pores with the diameter in the range 1.0 mm - 2.0 mm 35% of total pores and pores with the diameter larger than 2.0 mm - 35-45% of total pores (Tab.2).

Two experimental curves of the vertical force F versus CMOD for the concrete beams '1' and '2' are shown in Fig.6. The experimental curves are typical for concrete. They include an elastic range, hardening region, peak and softening region. The beam '2' was unloaded. The maximum vertical force F was equal to 1.94-2.18 kN (the tensile strength was 3.37-3.79 MPa).

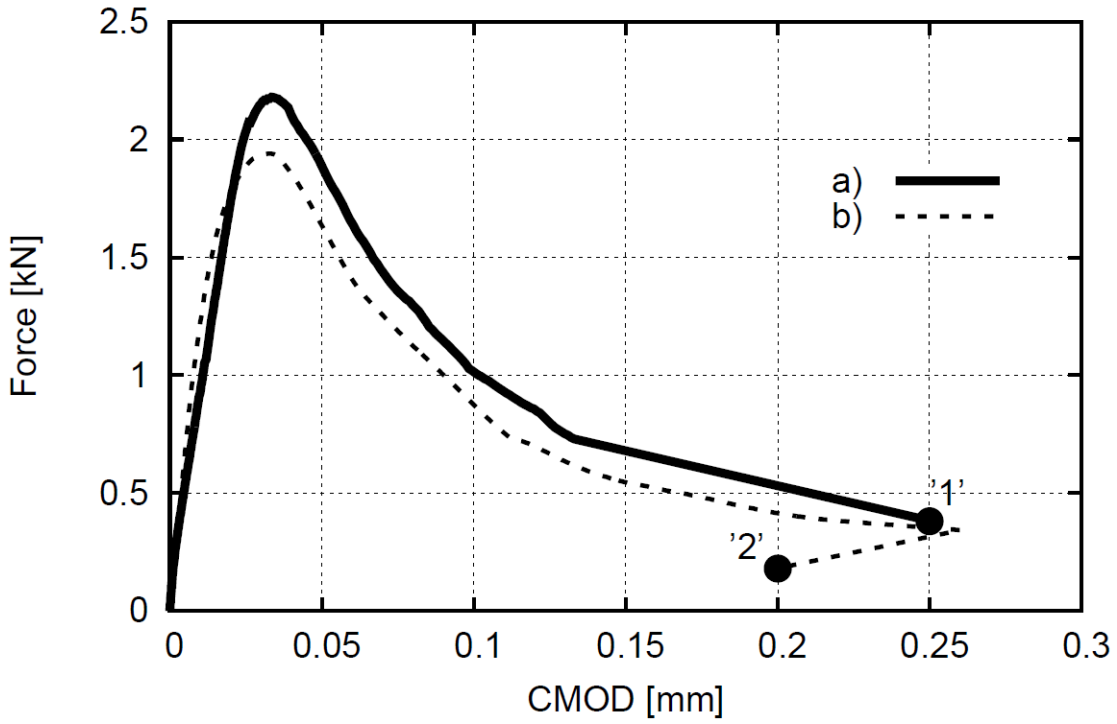

Fig.6: Experimental evolution of vertical force F against CMOD for two concrete beams: '1' (a) and '2' (b) (beam '2' was unloaded)

Figures 7 and 8 present the 3D micro-CT images of the beam '1' that was scanned under the residual force (point '1' on the curve of Fig.6). The 3D micro-CT images of the beam '2' that was unloaded for scanning (point '2' on the curve of Fig.6) are shown in Figs.9 and 10. In addition, the measured crack width w was also shown (along the beam height above the notch h and along the beam width b). The crack width was measured perpendicularly to the crack axis. The manual measurements were carried out at nine points. The final macro-crack was strongly curved along the beam depth and height due to the presence of aggregate particles (Figs.7-10). The shape and width of the macro-crack strongly varied along the beam height (due to bending) and depth (due to a heterogeneous nature of concrete). The cracks mainly propagated through the cement matrix and ITZs which were the weakest phase in concrete. The cracks also propagated through single weak aggregate particles [5] The micro-cracks occurred first in porous ITZs around aggregate particles and then they connected themselves through a bridging mechanism [5]. When two interfacial cracks occurred around adjacent aggregate particles, a crack inside the cement matrix initiated to bridge the interfacial cracks so that a connected crack path was formed. The cracks' branching also occurred [5]. The crack height h changed along the beam depth from h=31 mm up to h=33 mm. The distribution of the crack width in the beams '1' and '2' was qualitatively similar (Figs.8 and 10). The final crack width in the tensile region non-linearly decreased with the beam height from w_c=0.34 mm down to w_c=0.11 mm in the beam '1' and from w_c=0.26 mm down to w_c=0.06 mm in the beam '2' that was unloaded (Figs.8 and 10). The final crack width above the notch in the beam '1' changed with the depth from w_c=0.25 mm at the depth of 5 mm from the front side down to w_c=0.28 mm at the depth of 35 mm (Fig.9b). The final crack width above the notch in the beam '2' (that was unloaded) changed with the beam depth from w_c=0.10 mm at the depth of 10 mm from the front side up to w_c=0.26 mm at the depth of 30 mm. The largest crack width in the beam '1' (w_c=0.37 mm) was thus by about 30% higher than in the beam '2' (w_c=0.26 mm) due to the cracks' closure after unloading in the beam '2'.

Due to cracking, the clear changes of the volume of both pores and cracks happened (Tabs.2 and 3). The volume of pores and cracks in the beam '1' increased by 343.2 mm^3 during deformation (0.31%). The volume of closed pores slightly decreased from 2.26% up to 2.17% (reduction by 4%), and the volume of open pores strongly increased from 1.16% up to 1.56% (growth by 35%). In the beam '2' (that was unloaded), the growth of the volume of pores and cracks was apparently smaller and equal to 264.1 mm^3 (0.24%). The volume of closed pores slightly decreased from 2.40% down to 2.30% (reduction by 4%) and the volume of open pores strongly increased from 0.85% up to 1.19% (growth by 40%). The small reduction of the closed pores' volume was caused

by their incorporation into the cracks. The width of the fracture process zone may be accurately measured using the digital image correlation (DIC) technique [29-32]. The width of the fracture process zone on the front side of the concrete beam above the notch (for the similar concrete mix) using the DIC technique was w_{lz}=3.48 mm (1.74×d_{50}, 0.22×d_{max}) [5]. To measure the width of ITZs, the scanning electron microscope (SEM) may be used [33-35]. We used the microscope Hitachi TM3030 with the magnification factor of 30,000. The width of ITZs along the aggregate particles in the similar concrete mix on the front beam side during bending changed between 30 μm and 50 μm [5]. The maximum porosity of ITZs was at aggregates - 25% [23].

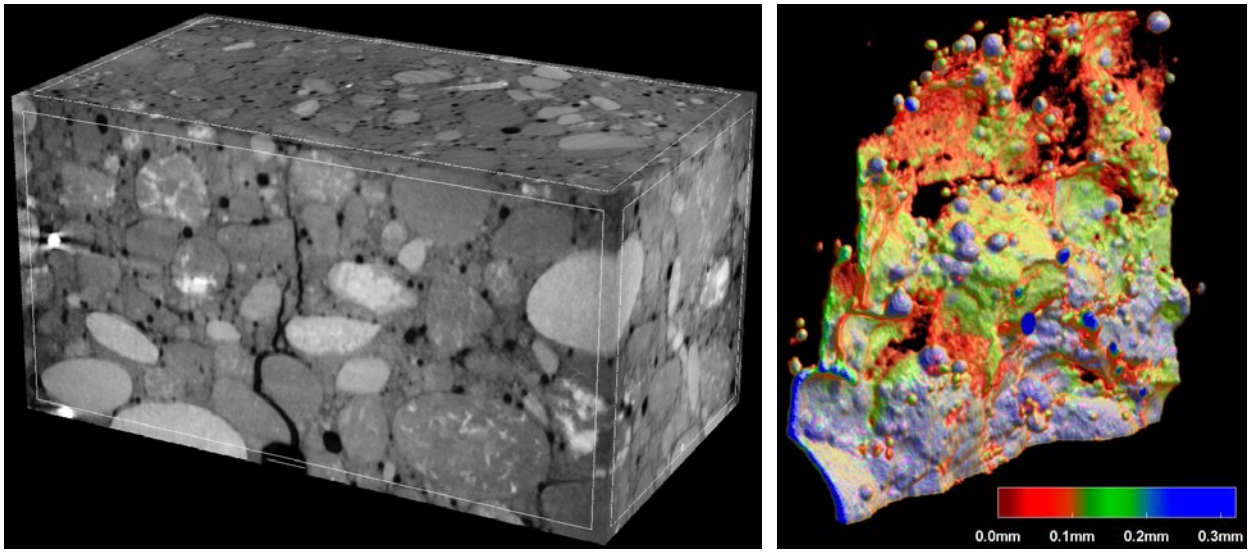

a) b)

Fig.7: 3D micro-CT image of cracked concrete beam '1' under existing residual force close to failure (point '1' on curve F=f(CMOD) of Fig.6): a) external view on front side of beam and b) macro-crack with width distribution between 0-0.3 mm (described by different colours)

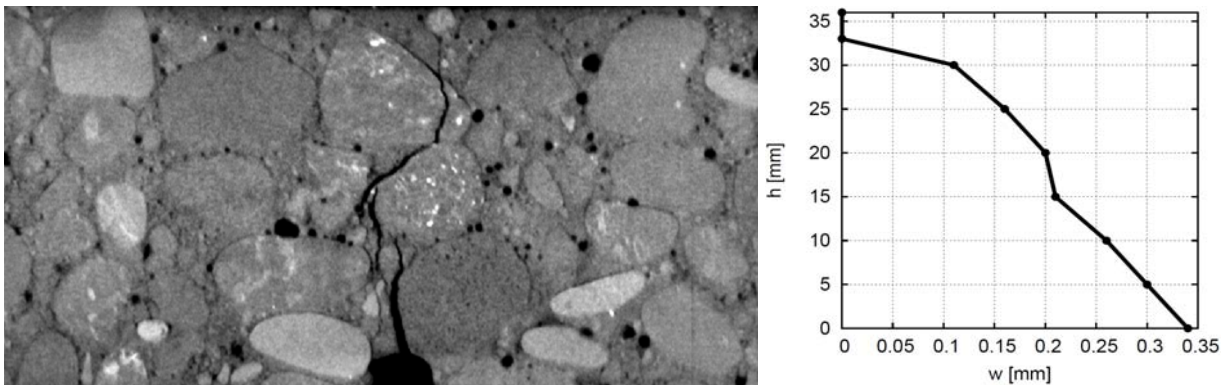

a)

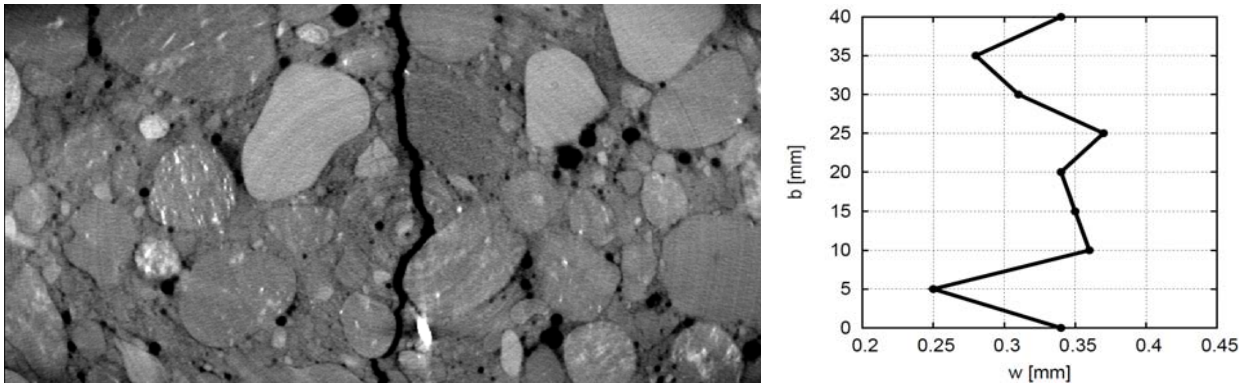

b)

Fig.8: Macro-crack in concrete notched beam '1' under existing residual force close to failure (point '1' on curve *F*=f(CMOD) of Fig.6): a) 2D micro-CT scan of vertical cross-section at depth of 20 mm from front side (mid-region) and b) 2D micro-CR scan of horizontal cross-section 1 mm above notch with measured crack width *w* along beam height above notch *h* or along beam width *b*

3.2 Evolution of fracture during continuous micro-CT scanning

Three experimental curves of the vertical force *F* versus CMOD for three concrete beams '1', '2' (Section 3.1) and '3' are shown in Fig.11. The greatest vertical force *F* was equal to 1.94-2.26 kN (the tensile strength was 3.37-3.93 MPa). The beam '3' was three times scanned by micro-CT: 1) before the peak load (point '1' in Fig.11), 2) after the peak load in the softening regime (point '2' in Fig.11) and 3) in the residual state (point '3' in Fig.11). No jumps were observed on the experimental curve during continuous deformation without unloading (caused by eventual relaxation and creep phenomena).

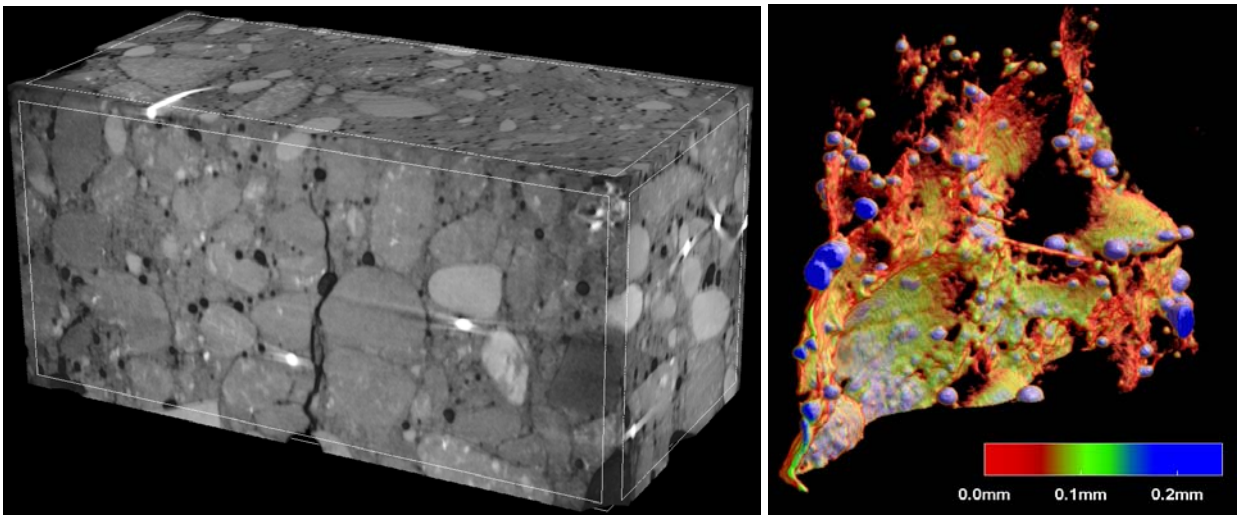

a) b)

Fig.9: 3D micro-CT image of cracked concrete beam '2' after unloading close to failure (point '2' on curve *F*=f(CMOD) of Fig.6): a) external view on front side of beam and b) macro-crack with width distribution between 0-0.2 mm (specified by different colours)

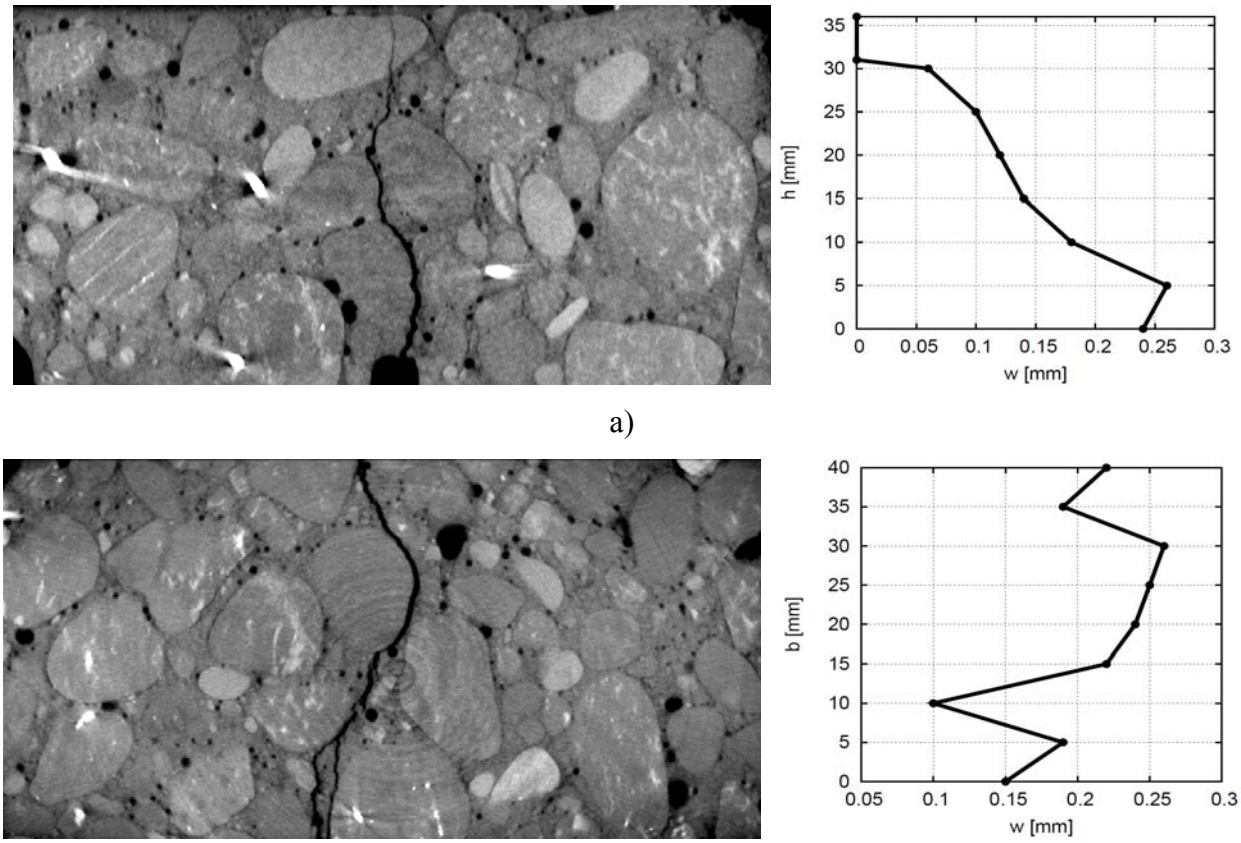

a)

b)

Fig.10: Macro-crack in concrete notched beam '2' after unloading close to failure (point '2' on curve *F*=f(CMOD) of Fig.6): a) 2D micro-CT scan of vertical cross-section at depth of 20 mm from front side (mid-region) and b) 2D micro-CR scan of horizontal cross-section 1 mm above notch with measured crack width *w* along beam height above notch *h* or along beam width *b*

Tab.3: Volume of pores and cracks in beams '1' and '2' close to failure

Beam number	Volume of pores and cracks [mm^3]	%-volume of pores and cracks [%]	%-volume of closed pores [%]	%-volume of open pores and cracks [%]	Volume of cracks [mm^3]	%-volume of cracks [%]
1	4105.6	3.73	2.17	1.56	343.2	0.31
2	3839.6	3.49	2.30	1.19	264.1	0.24

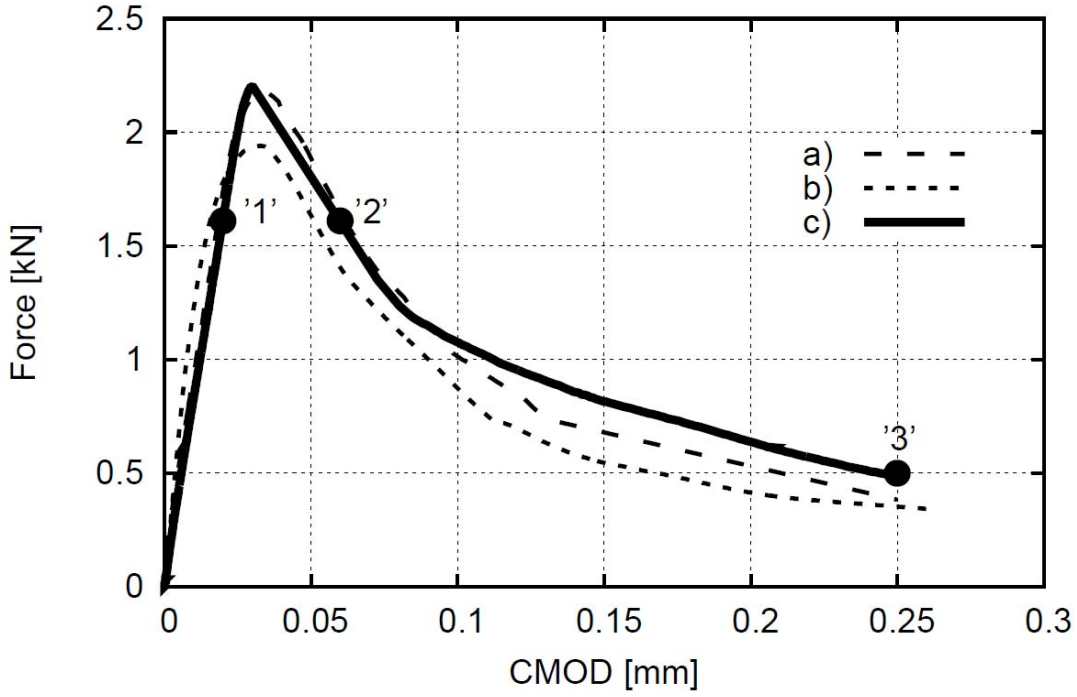

Fig.11: Experimental evolution of vertical force (F) against CMOD for three concrete beams: a) beam '1', b) beam '2' and c) beam '3' with marked micro-CT scanning points '1'-'3'

Figure 12 shows the external 3D micro-CT images of the concrete beam '3' for the different loading points: '1' with F=1.59 kN (about 70% of the peak force in the pre-peak regime) for CMOD=0.03 mm, '2' with F=1.61 kN (about 70% of the peak force in the post-peak regime) for CMOD=0.06 mm and '3' with F=0.50 kN (residual force, 20% of the peak force) for CMOD=0.25 mm. Table 4 includes the data on the volume changes of pores and cracks in the concrete beam '3'.

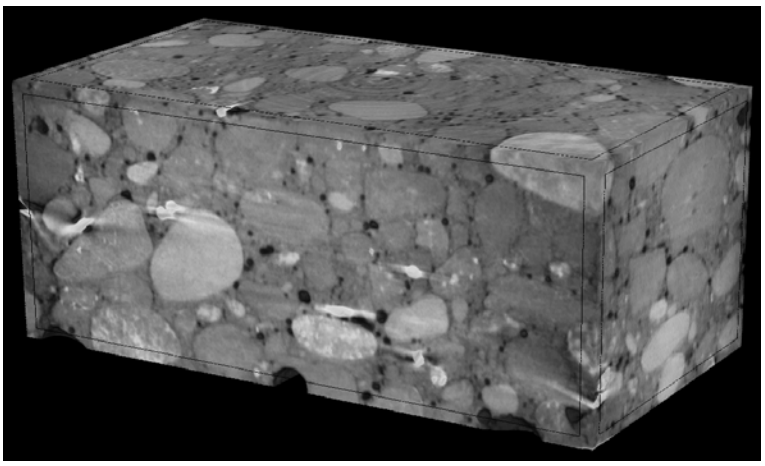

a)

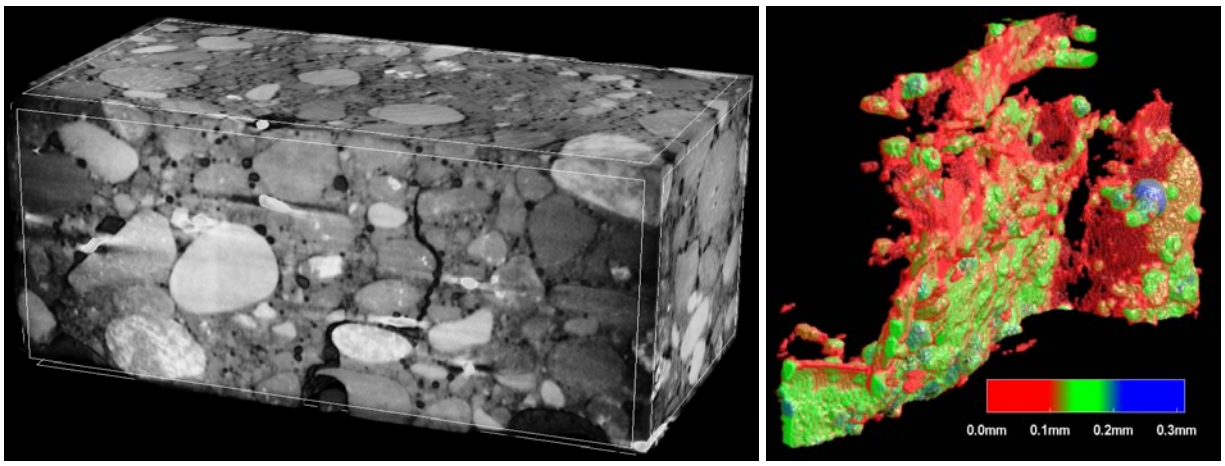

b)

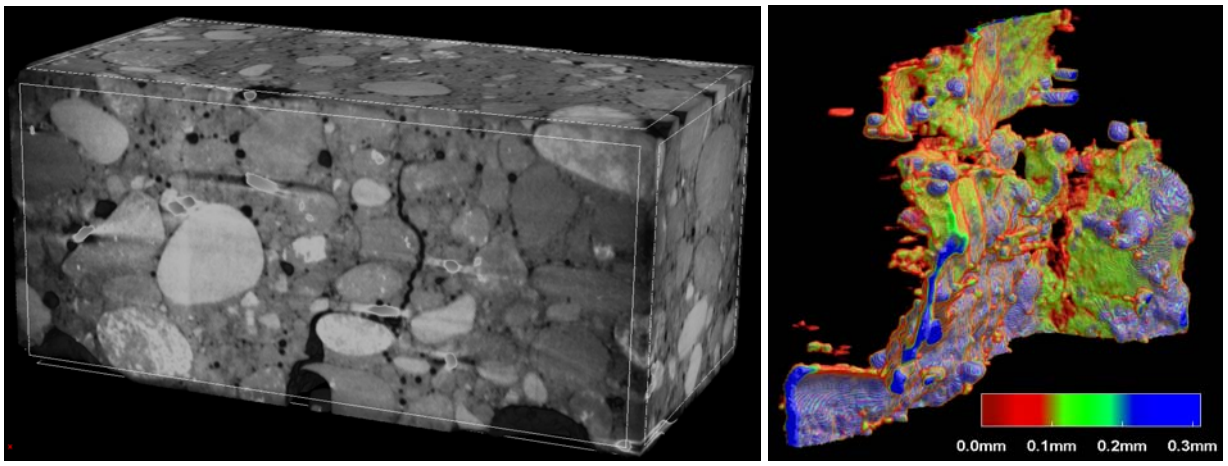

c)

Fig.12: Macro-crack in concrete beam '3' on 3D micro-CT image with crack' width distribution between 0 - 0.2/0.3 mm (represented by different colours): a) initial non-cracked beam, b) cracked beam for point '2' on curve *F*=f(CMOD) of Fig.11 and c) cracked beam for point '3' on curve *F*=f(CMOD) of Fig.11)

Tab.4: Volume of pores and cracks in concrete beam '3' for different loading points of Fig.11

Loading point	Volume of pores and cracks [mm^3]	%-volume of pores and cracks [%]	%-volume of closed pores [%]	%-volume of open pores and cracks [%]	Volume of cracks [mm^3]	%-volume of cracks [%]
'0' CMOD= 0.0 mm	4213.1	3.83	2.43	1.40	0	0
'1' CMOD= 0.03 mm	4232.2	3.85	2.42	1.43	19.1	0.02
'2' CMOD= 0.06 mm	4367.2	3.97	2.33	1.44	154.1	0.14
'3' CMOD= 0.25 mm	4653.6	4.23	2.15	2.08	440.5	0.40

The volume of pores and cracks in the entire non-cracked beam '3' before the test (point '0' in Tab.4) was 4213.1 mm^3 of the entire volume (3.83%: 2.43% (closed pores) and 1.40% (open pores and cracks)). For the point "1" of Fig.11, the insignificant volume changes of pores and cracks were obtained. A strain localization zone (FPZ) started to rapidly develop for 80-90% of the pre-peak load. Later, the localized zone changed into a macro-crack [5], [36]. In the point "2" of Fig.11, the volume of pores and cracks increased by about 3.5% up to 4367.2 mm^3 (3.97% of the total volume: 2.33% (closed pores) and 1.44% (open pores and cracks)). The cracks' volume was 154.1 mm^3 (0.14%). The largest crack width in the entire volume was w_c=0.20 mm (point '2'). For the point "3" of Fig.11, the volume of pores and cracks increased as compared to the point '2' by about 6.2% to 4653.6 mm^3 (4.23% of the total volume: 2.25% (closed pores) and 2.08% (open pores and cracks). The cracks' volume was 440.5 mm^3 (0.40%). The largest crack width in the entire volume was w_c=0.31 mm (point '3'), smaller by 20% than in the beam '1' due to larger initial global porosity (Tab.2) and higher by 20% than in the beam '2' due to continuous deformation process.

Figure 13 presents the evolution of the %-volume of pores and cracks (Tab.4). The evolution of fracture volume of cracks against CMOD (that was linearly prescribed) was composed of three clear linear regions with the different intensity: 1) region of micro-cracks (CMOD=0-0.03 mm), 2) transitional region (CMOD=0.03-0.06 mm) and 3) region of the macro-crack formation

(CMOD=0.06-0.25 mm). The largest normalized crack volume's growth (expressed by %-volume divided by CMOD) was in the transitional region.

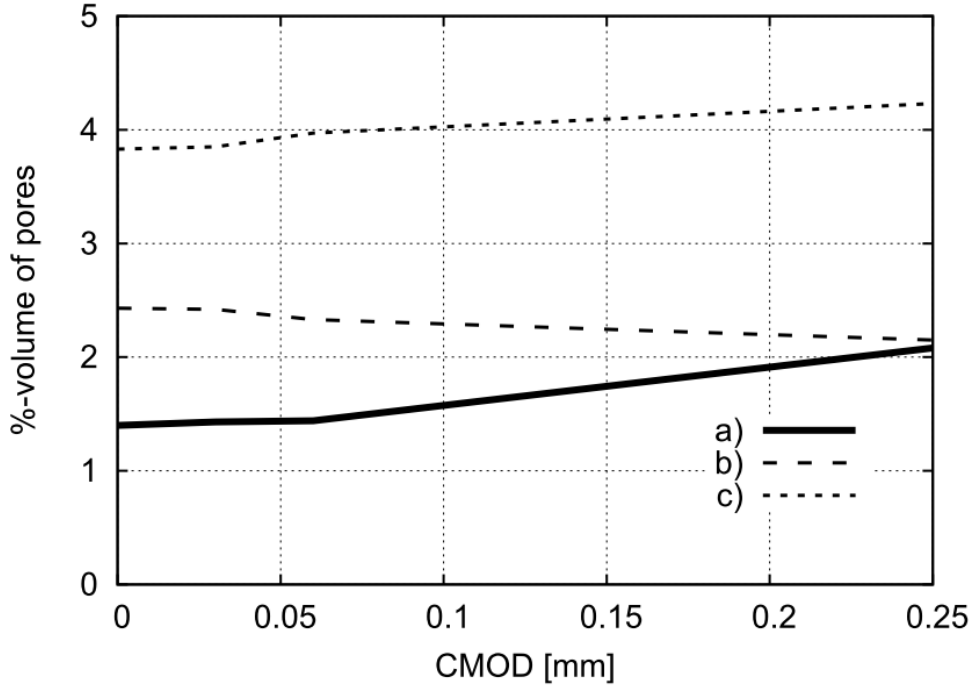

A)

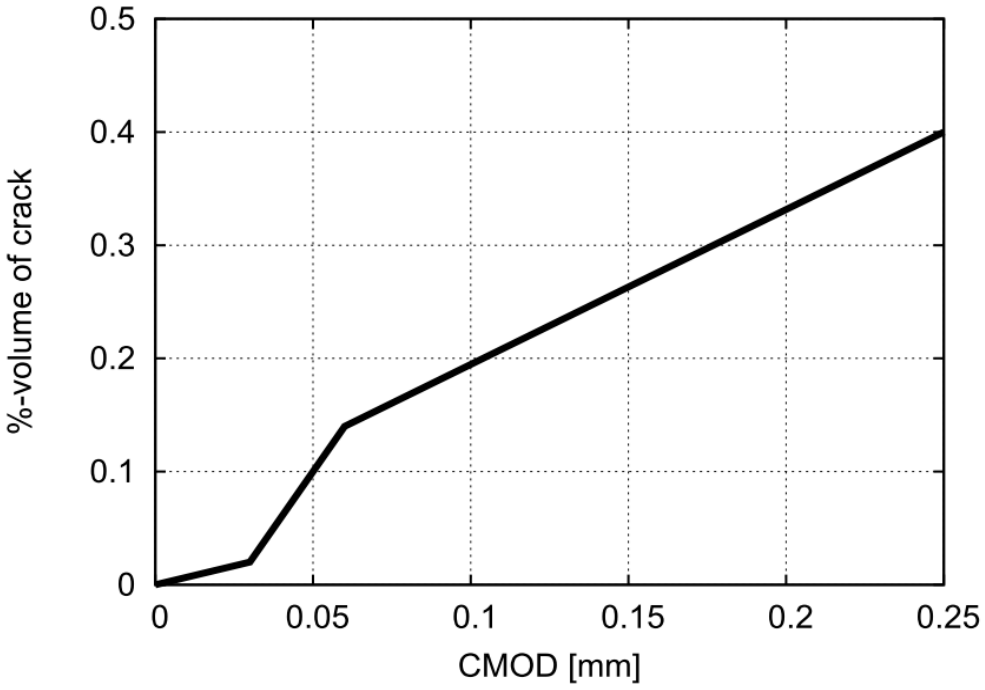

B)

Fig.13: Relationship between %-volume and CMOD during bending for beam '3': A) pores (a) open pores, b) closed pores and c) total pores) and B) cracks

The different horizontal and vertical cross-sectional micro-CT images (intersecting the beam centroid) for the points '2' and '3' of Fig.11 are demonstrated in Figs.14 and 15. The crack width in the tensile region non-linearly changed with the beam height from w=0.18 mm down to w=0.07 mm for the loading point '2' of Fig.11 and from w_c=0.28 mm down to w_c=0.10 mm for the loading point '3' of Fig.11 (Figs.14a and 15a). The crack width above the notch strongly changed along the beam depth from w=0.19 mm at the beam depth of 5 mm from the beam front side down to w_c=0.09 mm at the beam depth of 35 mm from the beam front side for the loading point '2' of Fig.11 (Fig.14b). The crack width above the notch for the loading point '3' of Fig.11 changed with the beam depth from w=0.25 mm at the depth of 5 mm from the beam front side down to w_c=0.15 mm at the beam depth of 35 mm (Fig.15b).

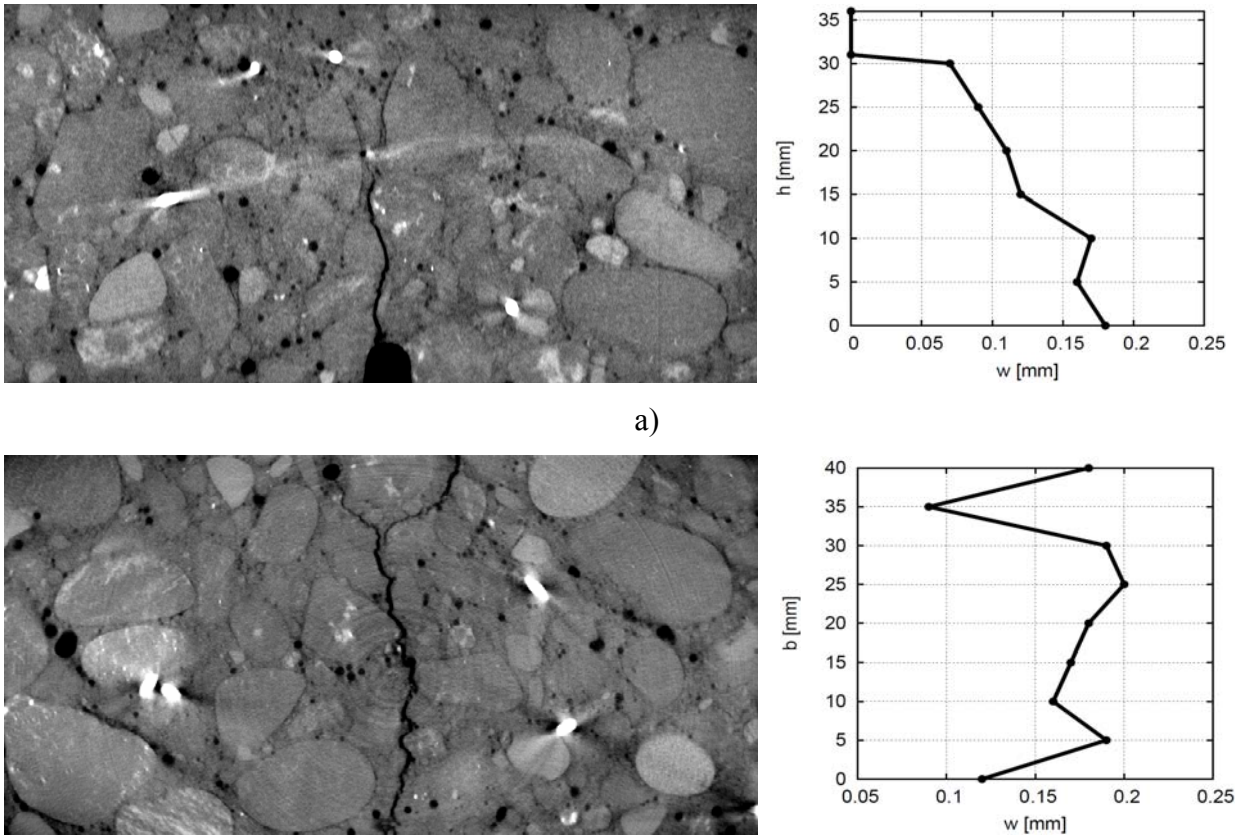

a)

b)

Fig.14: 2D micro-CT images of cracked beam '3' for loading point '2' of Fig.11: a) vertical cross-section and b) horizontal cross-section with measured crack width w along beam height above notch h and along beam width b

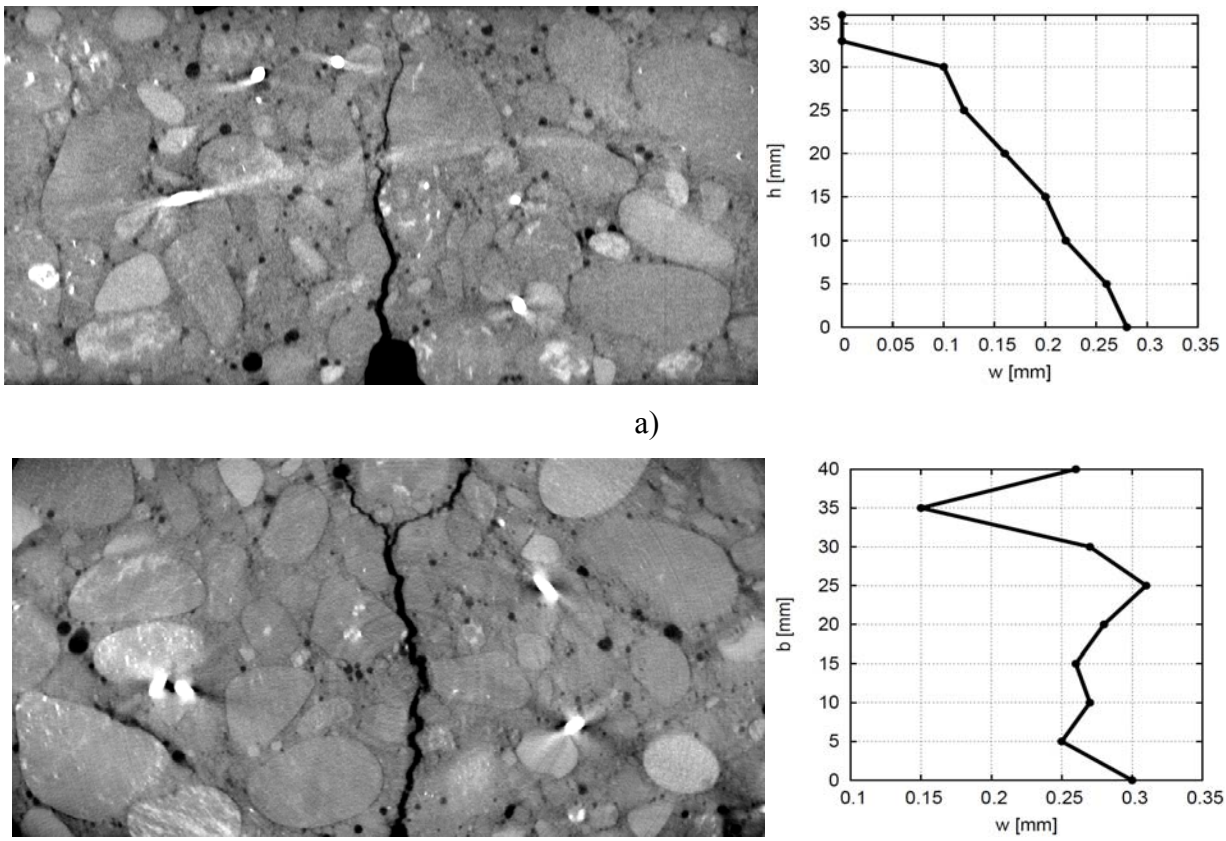

Fig.15: 2D micro-CT images of cracked beam '3' for loading point '3' of Fig.11: a) vertical cross-section and b) horizontal cross-section with measured crack width *w* along beam height above notch *h* and along beam width *b*

4. Conclusions

This paper presents the results of experimental research works aimed for the determining 3D fracture evolution in plain concrete beams under 3-point bending by the extended X-ray micro-CT system that is a powerful tool to visualize the internal damage of concrete specimens. The extended system allowed for continuous scanning during deformation without unloading breaks. The following conclusions can be offered:

- The maximum macro-crack width during continuous scanning (w_c=0.31-0.37 mm) was higher by about 20-30% than in the beam subjected to unloading (w_c=0.26 mm). The volume of cracks close to the failure force was 0.24% in the unloaded beam and 0.31-0.40% in the beams under the residual force (as compared to the total volume).

- The macro-crack was strongly curved in space caused by a stochastic aggregate location. First, the micro-cracks occurred in ITZs and propagated later through the cement matrix by bridging. The cracks propagated also through closed pores and occasionally through weak aggregate particles.

- For the force $0.7F_{max}$ only insignificant volume changes of cracks occurred in the pre-peak regime. Next, up to the force $0.7F_{max}$ in the post-peak regime, the volume of pores increased by about 3,5%, the crack volume was 154.1 mm^3 and maximum crack width was w_c=0.20 mm. Between $0.7F_{max}$ and $0.2F_{max}$ in the post-peak regime, the volume of pores increased by about 6,2% and the crack volume by about 300% to the value 440.5 mm^3. The maximum crack's width was w_c=0.31 mm shortly before the beam failure. The highest normalized crack intensity occurred in the region of the peak vertical load (for CMOD=0.03-0.06 mm).

- The initial volume of pores in non-cracked beams was equal to 3.25-3.83% of the entire beam volume. The initial open pores represented 0.85-1.40% and the initial closed pores represented 2.26-2.43% of the total volume. The pores with the diameter smaller than 1.0 mm constituted about 20-30%, pores with the diameter 1.0-2.0 mm represented about 35% and pores with the diameter larger than 2.0 mm formed about 35-45% of the total volume of pores in concrete beams.

Acknowledgements

Research work has been carried out as a part of the Project: "*Innovative resources and effective methods of safety improvement and durability of buildings and transport infrastructure in the sustainable development*" financed by the European Union (POIG.01.01.02-10- 106/09-01) and of the Project "*Effect of concrete meso-structure on initiation and propagation of cracks - experiments and two-scale numerical model*" financed by the National Science Centre (NCN) (UMO-2017/25/B/ST8/02108).

Data availability

The raw/processed data required to reproduce these findings cannot be shared at this time due to time limitations.

Declarations of interest: none.

References

[1] Bažant Z. and Planas J. (1998) *Fracture and size effect in concrete and other quasi-brittle materials*. CRC Press LLC, Boca Raton.

[2] Lilliu G. and van Mier J.G.M. (2003) 3D lattice type fracture model for concrete. *Engineering Fracture Mechanics* 70:927-941.

[3] Tejchman J. and Bobiński J. (2013) *Continuous and discontinuous modeling of fracture in concrete using FEM*. Springer, Berlin-Heidelberg.

[4] Tejchman J. and Kozicki J. (2010) *Experimental and theoretical investigations of steel-fibrous concrete.* Springer Series in Geomechanics and Geoengineering, Springer, Berlin-Heidelberg.

[5] Skarżyński Ł and Tejchman J. (2016) Experimental investigations of fracture process in concrete by means of X-ray micro-computed tomography. *Strain* 52:26-45.

[6] Vicente M.A., Mínguez J. and González D.C. (2017) Book chapter: the use of computed tomography explore the microstructure of materials in civil engineering: from rocks to concrete (in: Halefoglu A.M., editor) *Computed tomography - advanced applications*. InTech, pp. 207-230.

[7] Vicente M.A., Mínguez J., and Gonzalez D.C. (2019) Computed tomography scanning of the internal microstructure, crack mechanisms and structural behaviour of fiber-reinforced concrete under static and cyclic bending tests, *International Journal of Fatigue* 121:1-19.

[8] EN 12390-5:2009 Testing hardened concrete. Flexural strength of test specimens.

[9] Vicente M.A., Ruiz G., Gonzalez D.C., Mínguez J., Tarifa M. and Zhang X.X. (2018) CT-Scan study of crack patterns of fiber-reinforced concrete loaded monotonically and under low-cycle fatigue, *International Journal of Fatigue* 114:138-147.

[10] Chung S.Y., Abd Elrahman M., Stephan D. and Kamm P.H. (2018) The influence of different concrete additions on the properties of lightweight concrete evaluated using experimental and numerical approaches. *Construction and Building Materials* 189:314–322.

[11] Schock J., Liebl S., Achterhold K. and Pfeiffer F. (2016) Obtaining the spacing factor of microporous concrete using high-resolution Dual Energy X-ray Micro CT. *Cement and Concrete Research* 89:200-205.

[12] Liu T., Qin S., Zou D., Song W. and Teng J. (2018) Mesoscopic modeling method of concrete based on statistical analysis of CT images. *Construction and Building Materials* 192:429–441.

[13] Loeffler C.M., Qiua Y., Martin B., Heard W., Williams B., Niea X. (2018) Detection and segmentation of mechanical damage in concrete with X-ray microtomography. *Materials Characterization* 142:515-522.

[14] Nguyen T., Bui H., Tuan D., Ngo T., Nguyen G. (2017) Experimental and numerical investigation of influence of air-voids on the compressive behaviour of foamed concrete. *Materials & Design* 130:103–119.

[15] González D.C, Mínguez J., Vicente M.A., Cambronero F. and Aragón G. (2018) Study of the effect of the fibers' orientation on the post-cracking behavior of steel fiber reinforced concrete from wedge-splitting tests and computed tomography scanning. *Construction and Building Materials* 192:110–122.

[16] Ponikiewski T., Katzer J., Bugdol M. and Rudzki M. (2014) Determination of 3D porosity in steel fibre reinforced SCC beams using X-ray computed tomography. *Construction and Building Materials* 68: 333–340.

[17] Huang Y., Yang Z., Ren W., Liu G. and Zhang C. (2015) 3D meso-scale fracture modelling and validation of concrete based on in-situ X-ray Computed Tomography images using damage plasticity model. *International Journal of Solids and Structures* 67–68, 340-352.

[18] Tal D. and Fish, J. (2018) Stochastic multiscale modeling and simulation framework for concrete., *Cement and Concrete Composites* 90: 61-81.

[19] Yua Q., Liub H., Yanga, T. and Liua, H. (2018) 3D numerical study on fracture process of concrete with different ITZ properties using X-ray computerized tomography. *International Journal of Solids and Structures* 147: 204-222.

[20] Skarżyński Ł., Nitka M. and Tejchman J. (2015) Modelling of concrete fracture at aggregate level using FEM and DEM based on X-ray μCT images of internal structure, *Engineering Fracture Mechanics* 147: 13-35.

[21] Suchorzewski J., Tejchman J. and Nitka M. (2018) DEM simulations of fracture in concrete under uniaxial compression based on its real internal structure, *International Journal of Damage Mechanics* 27(4): 578-607.

[22] Suchorzewski J., Tejchman J. and Nitka M. (2018) Experimental and numerical investigations of concrete behaviour at meso-level during quasi-static splitting tension. *Theoretical and Applied Fracture Mechanics* 96: 720-739.

[23] Suchorzewski J., Tejchman J., Nitka M. and Bobiński J. (2019) Meso-scale analyses of size effect in brittle materials using DEM. *Granular Matter* 21(9): 1-19.

[24] Skarżyński Ł. and Suchorzewski J. (2018) Mechanical and fracture properties of concrete reinforced with recycled and industrial steel fibers using Digital Image Correlation technique and X-ray micro computed tomography. *Construction and Building Materials* 183: 283-299.

529 [25] Skarżynski Ł., Marzec I. and Tejchman J. (2018) Crack evolution in concrete compressive
530 fatigue experiments based on X-ray micro-CT images. *International Journal of Fatigue* 122: 256-
531 272.
532 [26] Nitka M. and Tejchman J. (2018) A three-dimensional meso scale approach to concrete fracture
533 based on combined DEM with X-ray μCT images, *Cement and Concrete Research,* 107: 11-29.
534 [27] Trawiński, W., Bobiński, J. and Tejchman, J. (2016) Two-dimensional simulations of concrete
535 fracture at aggregate level with cohesive elements based on X-ray micro-CT images. *Engineering*
536 *Fracture Mechanics* 168: 201-226.
537 [28] Trawiński, W., Tejchman, J., Bobiński, J. (2018) A three-dimensional meso-scale approach
538 with cohesive elements to concrete fracture based on X-ray μCT images. *Engineering Fracture*
539 *Mechanics* 189: 27-50.
540 [29] Skarżyński Ł, Kozicki J, Tejchman J. (2013) Application of DIC technique to concrete - study
541 on objectivity of measured surface displacements. *Experimental Mechanics* 53: 1545-1559.
542 [30] Corr, G., Accardi, M., Graham-Brady, L. and Shah, S. (2007) Digital image correlation
543 analysis of interfacial debonding properties and fracture behavior in concrete. *Engineering Fracture*
544 *Mechanics* 74: 109-121.
545 [31] Wu, Z., Rong, H., Zheng, J. and Dong, W. (2011) An experimental investigation on the FPZ
546 properties in concrete using digital image correlation technique. *Engineering Fracture Mechanics*,
547 78: 2978-2990.
548 [32] Alam, S. Y., Loukili, A. and Grondin, F. (2012) Monitoring size effect on crack opening in
549 concrete by Digital Image Correlation. *European Journal of Environmental and Civil Engineering*
550 16: 1-19.
551 [33] Nemati, K. M. (1997) Fracture analysis of concrete using scanning electron microscopy,
552 *Scanning* 19: 426-430.
553 [34] Balendran, R. V., Pang, H. W. and Wen, H. X. (1998) Use of scanning electron microscopy in
554 concrete studies. *Structural Survey* 16: 146-153.
555 [35] Hadjab, S. H, Chabaat, M., Thimus, J. F. (2007) Use of Scanning Electron microscope and the
556 non-local isotropic damage model to investigate fracture process zone in notched concrete beams.
557 *Experimental Mechanics* 47: 473–84.
558 [36] Skarżyński, Ł. and Tejchman, J. (2013) Experimental investigations of fracture process in plain
9 and reinforced concrete beams under bending. *Strain* 49(6): 521-543